submitted to *Geophys. J. Int.*

Surface deformations caused by pressurized finite ellipsoidal cavities

Mehdi Nikkhoo[1,2] and Eleonora Rivalta[1,3]

[1] *GFZ German Research Centre for Geosciences, Potsdam, Germany. E-mail: mehdi.nikkhoo@gfz-potsdam.de*

[2] *The Abdus Salam International Center for Theoretical Physics, Trieste, Italy,*

[3] *Department of Physics and Astronomy, Alma Mater Studiorum University of Bologna, Italy.*

SUMMARY

We develop solutions for the surface deformation field due to the pressurization of a finite (triaxial) ellipsoidal cavity in a half-space. The solution is in the form of a non-uniform distribution of triaxial point sources within the cavity. The point sources have the same aspect ratio, determined by the cavity shape, while their strengths and spacing are determined in an adaptive manner, such that the net point-source potency per unit volume is uniform. We validate and compare our solution with available analytical and numerical solutions. We provide computationally-efficient MATLAB codes tailored for source inversions. This solution opens the possibility of exploring potential deviations of magma chambers from axi-symmetric geometries.

Key words: Geomechanics; Kinematics of crustal and mantle deformation; Physics of magma and magma bodies; Volcano monitoring.

1 INTRODUCTION

Volcano deformation models are idealized representations of magmatic intrusions or pressurized magma chambers. Through fitting these models to geodetic data measured at the Earth's surface, the shape, location, spatial orientation and volume change of pressurized magma chambers can be constrained

from (Dvorak & Dzurisin 1997; Dzurisin 2003; Lisowski 2007; Segall 2010). The surface displacements caused by deep volumetric deformation sources can be adequately modelled through point-source models such as the point spherical (Mogi 1958), point spheroidal (Davis et al. 1974) and point ellipsoidal (Davis 1986) models. A triaxial point-source model that includes the mentioned solutions as special cases is the point Compound Dislocation Model (point CDM Nikkhoo et al. 2017), which is composed of three mutually orthogonal point tensile dislocations (see also Lisowski et al. 2008; Bonafede & Ferrari 2009).

McTigue (1987); Yang et al. (1988) showed that point sources fail to properly simulate the near-field surface displacements associated with shallow pressurized cavities. This is because the near-field displacements are affected by the finite dimension of the source. Finite source models are required to constrain all source parameters reliably (Lisowski 2007; Segall 2010). The most common finite source models of uniform pressure are the finite spherical (McTigue 1987), finite spheroidal (Yang et al. 1988) and penny-shaped crack Sun (1969); Fialko et al. (2001) models. These models are all special cases of a pressurized ellipsoid.

After Eshelby (1957), a solution for a uniformly pressurized finite ellipsoidal cavity in the full space can be obtained by appropriate triaxial point sources uniformly distributed throughout the cavity (Yang et al. 1988; Segall 2010). Davis et al. (1974); Davis (1986) incorporated the Mindlin (1936) half-space Green's functions instead of the full-space Green's functions into the Eshelby's solution to derive their approximate half-space point-source solution. Similarly, Yang et al. (1988) used the half-space Green's functions to develop a solution for finite spheroids. Yang et al. (1988) also showed that, as a rule of thumb, the solution is accurate if the depth to the top of the spheroid is larger than the radius of curvature at the spheroid top. Amoruso & Crescentini (2011) and Amoruso & Crescentini (2013) used the Eshelby's solution together with a quadrupole expansion of the half-space Green's functions to obtain generic finite ellipsoidal source models. These models can be applied only to sources at intermediate depths. Solutions appropriate for shallow ellipsoidal sources along with computer programs suitable for inversions are yet to be developed and adopted by the community.

Following Eshelby (1957) and Davis et al. (1974); Davis (1986), it is straightforward to derive a half-space solution for finite ellipsoids as an evenly-spaced distribution of triaxial point sources. Such an approach is, however, impractical for inversions, as it would involve a very large number of point sources to achieve good accuracy for shallow cavities. Here we develop an equivalent, adaptive solution in the form of a non-uniform distribution of triaxial point sources, that is point CDMs, with depth-dependent spacing and strengths. We first introduce an adaptive algorithm that involves a set of analytical solutions controlling the location, spacing and strengths of the point CDMs. Next, we compare our solutions with published analytical and numerical solutions.

2 METHODS

2.1 A new adaptive configuration

In the following we develop a solution for uniformly pressurized ellipsoidal cavities in a homogeneous, linear, elastic half-space with Poisson's ratio, ν, and bulk modulus, K. We refer to this solution as the finite Ellipsoidal Cavity Model (finite ECM). We adopt a Cartesian right-handed xyz coordinate system with the origin on the free surface and the z axis pointing upward. The parameters defining a finite ECM are: the coordinates of its center $(x_0, y_0, -d_\mathrm{C})$, where d_C is the depth to the center of the cavity, the semiaxes (a_x, a_y, a_z), the rotation angles $(\omega_x, \omega_y, \omega_z)$ and the overpressure δp. If the rotation angles are zero, a_x, a_y and a_z are aligned with the x, y and z axes, respectively.

Nikkhoo et al. (2017) showed that the far-field deformations due to any ellipsoidal cavity can be represented by a point CDM located at the cavity center and having potencies

$$\begin{pmatrix} \Delta V_x \\ \Delta V_y \\ \Delta V_z \end{pmatrix} = \frac{-V\delta p}{3K}(\mathbf{S} - \mathbf{I}_3)^{-1} \begin{pmatrix} 1 \\ 1 \\ 1 \end{pmatrix}, \tag{1}$$

where $V = \frac{4\pi}{3} a_x a_y a_z$ is the volume of the cavity, $\mathbf{I_3}$ is the identity matrix and

$$\mathbf{S} = \begin{pmatrix} S_{1111} & S_{1122} & S_{1133} \\ S_{2211} & S_{2222} & S_{2233} \\ S_{3311} & S_{3322} & S_{3333} \end{pmatrix},$$

where S_{iijj} are the Eshelby (1957) tensor components, with the indices 1, 2 and 3 indicating the x, y and z directions, respectively. The terms S_{iijj} are nonlinear functions of a_x, a_y, a_z and ν (see Eshelby 1957; Amoruso & Crescentini 2009; Segall 2010). This far-field solution is equivalent to the Davis (1986) point ellipsoidal source. The point-source approximation is accurate if the distance between the cavity and the observation points—here the depth of the cavity—is much larger than the characteristic dimension of the cavity. The approximation error is, thus, a function of the depth to semi-major axis ratio (McTigue 1987; Fialko et al. 2001; Segall 2010), which we denote in the following as c_r.

Following Eshelby (1957), the near-field deformations of a finite ellipsoidal cavity can be represented by a set of point CDMs—with potencies proportional to those in equation 1—continuously distributed throughout the cavity. Each point CDM of the set can be interpreted as an "auxiliary ellipsoid", that is, an infinitesimal ellipsoidal cavity with the same aspect ratio, pressure and spatial orientation as the finite cavity. In practice, a finite number of point CDMs can approximate the near-field solution with arbitrary accuracy. By trial and error we found that satisfactory results are achieved if: 1) the point CDM spacing is such that the auxiliary ellipsoids are regularly packed (ellipsoids tan-

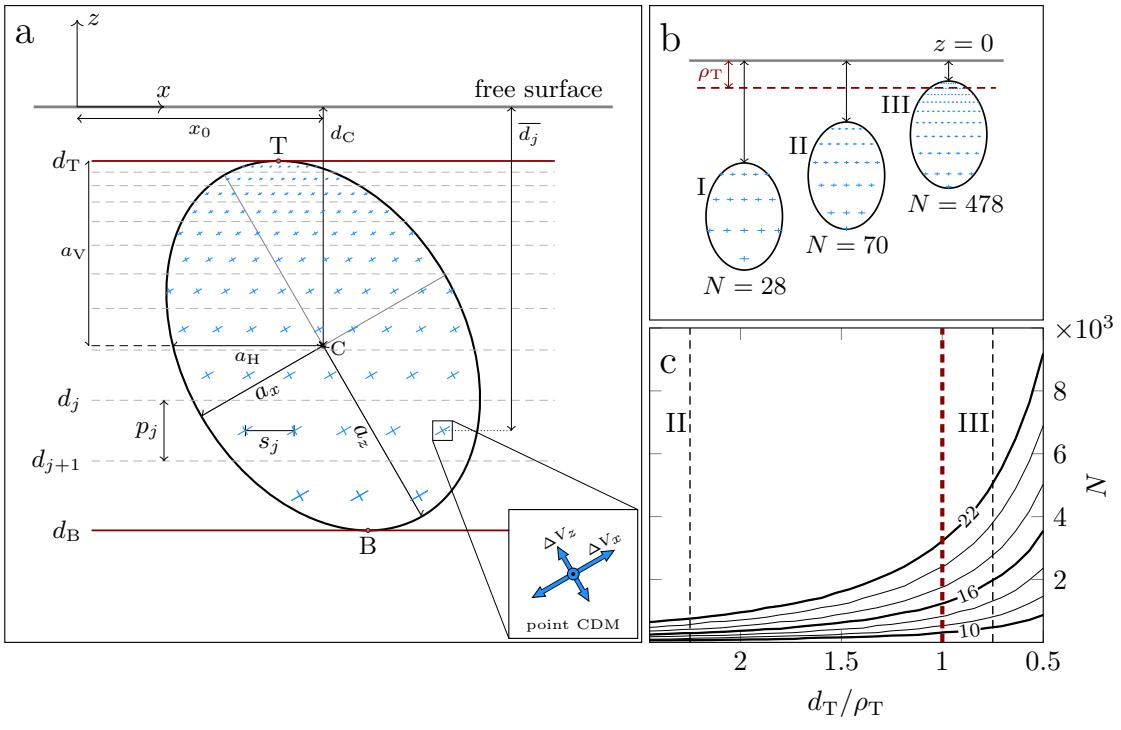

Figure 1. a) The adaptive source model for $c_r^* = 10$. The ellipsoid parameters are: center at $(x_0, 0, -d_C)$, $a_x/a_z = 0.714$, $a_z/d_C = 0.826$, $\omega_x = \omega_z = 0°$ and $\omega_y = 30°$. d_T and d_B are the depths to the ellipsoid top (T) and bottom (B), respectively. $d_T/d_C = 0.226$ and $d_B/d_C = 1.774$. Red lines: uppermost and lowermost partitioning planes. The j-th partition is bounded by the ellipsoid and partitioning planes (dashed lines) at depths d_j and d_{j+1}. Cross symbols are the point CDMs, with a total number $N = 879$. Inset: point CDM configuration. For this ellipsoid geometry and for $\nu = 0.25$, $\Delta V_z/\Delta V_x = 0.671$. b) Adaptive source model ($c_r^* = 10$) for the same ellipsoid as in a) but with $\omega_x = \omega_y = \omega_z = 0°$. a_z/d_C is 0.344, 0.466 and 0.724 for I, II and III, respectively. d_T/ρ_T is 3.75, 2.25 and 0.85 for I, II and III, respectively. c) For the same source geometry as in panel b), the solid curves show N, for c_r^* varying between 10 and 22, as a function of d_T/ρ_T. Numbers on the thick curves indicate c_r^*. The vertical dashed line is $d_T = \rho_T$, which represents the Yang et al. (1988) rule of thumb. Note that for the tilted cavity in a) $\rho_T/a_z = 0.620$, whereas for the cavities in b) we have $\rho_T/a_z = 0.510$

.

gent to each other at the tips of their axes), and 2) the c_rs associated with the auxiliary ellipsoids are larger than a certain threshold, c_r^*, which we refer to as the "grid-spacing parameter" (section 2.3). Thus, if the semi-axes of the auxiliary ellipsoids are $a'_x = ka_x$, $a'_y = ka_y$, $a'_z = ka_z$, where $k < 1$ is a scale factor, the spacing between the point CDMs in the three directions becomes $2ka_x$, $2ka_y$, $2ka_z$, respectively. Denoting the depth to the top and bottom of the ellipsoidal cavity with d_T and d_B, respectively, and defining $a_V = (d_B - d_T)/2$ (Fig. 1a), the c_r for the shallowest auxiliary ellipsoid will

be

$$c_{\mathrm{r}} = \frac{d'_{\mathrm{C}}}{a'_{\mathrm{C}}} = \frac{d_{\mathrm{T}} + k a_{\mathrm{V}}}{k a_{\mathrm{C}}}, \tag{2}$$

where d'_{C} and a'_{C} are the depth to the center and semi-major axis of the shallowest auxiliary ellipsoid, respectively. We note that $2a_{\mathrm{V}}$ is the vertical extent of the cavity and $2ka_{\mathrm{V}}$ is the vertical extent of the auxiliary ellipsoids. For a given c^*_{r}, equation 2 can be solved for k, which determines the point CDM spacing. The potencies of the point CDMs in this configuration are $(\Delta V_x/N, \Delta V_y/N, \Delta V_z/N)$, where ΔV_x, ΔV_y and ΔV_z are calculated from equation 1 and N is the total number of the point CDMs. Numerical convergence tests show that $c^*_{\mathrm{r}} =\sim 10$ provides very good results (see section 2.3), but it may lead to a large N and thus, long computation times.

To address this problem, we have devised a new configuration in which the size of the auxiliary ellipsoids increases with depth such that they all have the same c_{r}. In this new configuration the auxiliary ellipsoids are regularly packed in horizontal layers stacked on top of each other. The vertical extent of the layers—that is, the vertical extent of the auxiliary ellipsoids—are obtained from top to bottom through an iterative procedure. Assuming $c_{\mathrm{r}} = c^*_{\mathrm{r}}$, from equation 2 we have $k_1 = d_{\mathrm{T}}/(c^*_{\mathrm{r}} a_{\mathrm{C}} - a_{\mathrm{V}})$, which results in the vertical extent of the first layer being $2k_1 a_{\mathrm{V}}$. The depth to the top of the second layer is then $d_2 = d_{\mathrm{T}}(1 + 1/n_{\mathrm{p}})$, where $n_{\mathrm{p}} = d_{\mathrm{T}}/(2k_1 a_{\mathrm{V}})$. Using d_2 in place of d_{T}, and the same c^*_{r}, in equation 2, we determine k_2 and thus, the vertical extent of the second layer. By repeating this procedure, we determine the depths, and thus the vertical extents, of further layers. Now we determine the point CDM spacing and potencies in each layer. Let a_{H} and a_{h} denote the semi-major axis and semi-minor axis, respectively, of the horizontal ellipse formed by the intersection of the ellipsoidal cavity and a horizontal plane passing through its center. The spacing of the point CDMs in the j-th layer will be $2k_j a_{\mathrm{H}}$ and $2k_j a_{\mathrm{h}}$ in the directions parallel to a_{H} and a_{h}, respectively. Finally, we adjust the point CDM potencies in each layer such that the potency per unit volume remains uniform throughout the cavity.

The new configuration is obtained through the following adaptive algorithm:

1. We set c^*_{r} depending on the desired accuracy or the maximum total number of allowed point CDMs, N_{max}.
2. We determine d_{T} and d_{B} analytically (Appendix A).
3. We partition the cavity by using the planes $z = -d_{\mathrm{T}}$, $z = -d_{\mathrm{B}}$ and $z = -d_j$, where $d_j = d_{\mathrm{T}}\left(1 + 1/n_{\mathrm{p}}\right)^{j-1}$, $j = 2, 3, \ldots, M-1$ (dashed lines in Fig. 1a) in which M is the number of partitioning planes.
4. We calculate the volumes V_j of the cavity partitions analytically (see Appendix B).
5. We determine analytically the ellipses formed by the intersections of the cavity and the planes

$z = -\overline{d_j} = -(d_j + d_{j+1})/2$ passing through the middle of the partitions (see Fig. 1a and Appendix C).

6. On every intersection ellipse we create a regular grid of point CDMs such that one point CDM lies at the center of the ellipse (Fig. 1a). As the grid spacing parallel to a_{H} and a_{h} we use $s_j^{\mathrm{H}} = 2k_j a_{\mathrm{H}}$ and $s_j^{\mathrm{h}} = 2k_j a_{\mathrm{h}}$, respectively, where $k_j = d_j/(c_{\mathrm{r}}^* a_{\mathrm{C}} - a_{\mathrm{V}})$. N_j and N denote the total number of point CDMs within the j-th partition and within the cavity, respectively. Note that every partition will contain at least one point CDM at its center.
7. For the top and bottom partitions, we calculate h_i', for $i = 1, \ldots, N_j$, as the vertical distance between each point CDM and the cavity surface.
8. We set the potencies of the point CDMs as $(\alpha_{ij}\frac{V_j}{V}\Delta V_x, \alpha_{ij}\frac{V_j}{V}\Delta V_y, \alpha_{ij}\frac{V_j}{V}\Delta V_z)$, where for the top and bottom partitions ($j = 1$ and $j = M - 1$) $\alpha_{ij} = h_i / \sum_{k=1}^{N_j} h_k$ in which $h_i = h_i' + k_j a_{\mathrm{V}}$, and for all the other partitions $\alpha_{ij} = 1/N_j$.
9. We calculate $\gamma = d_{\mathrm{T}}/\rho_{\mathrm{T}}$, where ρ_{T} is the maximum radius of curvature at T (Appendix D) for further assessment of the solution quality.

For a specific c_{r}^* in this adaptive algorithm, N is determined by the shape (aspect ratio and size), depth and spatial orientation of the cavity (Fig. 1a-c). The link between the cavity depth and N can be better seen in Fig. 1b-c, where a varying depth for cavities of the same shape and orientation leads to different Ns.

N becomes very large when the source gets very shallow, but we have to keep in mind that ρ_T defines, as a rule of thumb, a minimum depth for the finite ECM model (see Yang et al. 1988, and Discussion). For cavities with $d_T \geq \rho_T$ (cavity top below the dashed line in Fig 1b), N does exceed a few thousands, even for $c_{\mathrm{r}}^* = 22$ (left-hand side of the red dashed line in Fig 1c), which is much larger than what is needed for an excellent solution (Section 2.3).

2.2 Computational efficiency of the finite ECM

The adaptive configurations have a substantially smaller N in comparison to evenly-spaced (uniform) configurations of equivalent accuracy. For example for the cavity in Fig 1a, the N for the evenly-spaced configuration of equivalent accuracy is 21.5 times larger than the N for the adaptive configuration. Similar factors calculated for the first (I), second (II) and third (III) cavities in Fig 1b are 1, 2.7, 14.4, respectively. Thus, the shallower is the cavity, the higher is the computational efficiency achieved by using the adaptive configuration in comparison with the evenly-spaced configuration.

The finite ECM involves computing the surface displacements for N point CDMs on the same grid of observation points. Thus, similar to Beauducel et al. (2020), we achieved further computational efficiency through a full vectorization of the original point CDM computer codes. As an exam-

ple, the computation of surface displacements at 100 observation points caused by a configuration of $N = 1000$ point CDMs requires 0.12 seconds on a personal computer (with 2.80 GHz processor with 8 threads). Using the adaptive algorithm along with the vectorization renders the finite ECM suitable for source inversions, akin to a conventional analytical solutions.

2.3 Calibration of the grid-spacing parameter

As stated earlier, the accuracy of the solution depends on c_{r}^*. In order to calibrate c_{r}^*, we use the only exact solution for finite non-spherical sources, namely, the Yang et al. (1988) solution for spheroidal cavities. We conduct systematic comparisons between the finite ECM and the Yang et al. (1988) surface displacements for ~ 7500 oblate and prolate spheroids with various aspect ratios, depths and dip angles (see caption of Table 1). To do so, we calculate the surface displacements associated with the Yang et al. (1988) solution on a regular grid of points using the MATLAB codes provided by Cervelli (2013) and Battaglia et al. (2013). Next, on the same grid, we calculate the surface displacements using the finite ECM for various c_{r}^*. As measures of the deviation between the two solutions we calculate $\epsilon_x = \max\{(u_x^{(1)} - u_x^{(2)})/u_z^{(2)}\}$ and $\epsilon_z = \max\{(u_z^{(1)} - u_z^{(2)})/u_z^{(2)}\}$, where the "$\max$" is calculated over all observation points, superscript "(1)" refers to the finite ECM and superscript "(2)" refers to the Yang et al. (1988) solution. We evaluate both the maximum of these deviations among all models, and the fraction of models where ϵ_x and ϵ_z are below 0.01. In order to avoid errors due to normalizing by near-zero vertical displacements, we limit the calculation to observation points with a vertical displacement larger than 10 per cent of the maximum vertical displacement on the grid. Results confirm that already with $c_{\mathrm{r}}^* = 10$ a very good accuracy is obtained. An excellent accuracy, sufficient for most practical applications, is reached with $c_{\mathrm{r}}^* = 12$ for prolate sources and $c_{\mathrm{r}}^* = 14$ for oblate sources. Convergence tests comparing the finite ECM solutions with an increasing c_{r}^* lead to similar results for triaxial cavities (see Table 1).

2.4 The volume change and the compressibility associated with the finite ECM

In order to fully characterize a volcano deformation source, it is critical to provide the practical means to calculate the volume change upon pressurization. The volume change is a measure of the source strength and can be used to estimate other important quantities such as the chamber compressibility, defined as the relative volume change for a unit pressurization. The chamber compressibility, together with the magma compressibility, is critical to estimate the real intrusion volume.

The volume change associated with ellipsoidal sources in a full space can be calculated from the Eshelby (1957) solution (see Amoruso & Crescentini 2009). This "full-space" volume change is also used as an approximation for the half-space models. This is because the exact volume change in

Table 1. Systematic comparison of the Yang et al. (1988) solution (prolate and oblate spheroids) with the finite ECM for varying c_{r}^*, and convergence test of the finite ECM for triaxial ellipsoids. $\overline{t_C}$ is the mean computation time, $\max \epsilon_x$ and $\max \epsilon_z$ are the maximum relative errors for the u_x and u_z components of the surface displacements, respectively, and $\alpha(\epsilon_x < 0.01)$ and $\alpha(\epsilon_z < 0.01)$ are the percentages of cases with relative errors below 1 per cent. The comparison involves 3800 prolate spheroids with parameters $x_0 = y_0 = 0\,\mathrm{m}$, $d_{\mathrm{C}} \in [100, 1000]\,\mathrm{m}$, $a_z = 1000\,\mathrm{m}$, $a_x = a_y \in [50, 950]\,\mathrm{m}$, $\omega_x = \omega_z = 0°$, $\omega_y \in [0°, 90°]$. For $c_{\mathrm{r}}^* = 10$, we have $N_{\mathrm{min}} = 20$, $N_{\mathrm{max}} = 2884$, whereas for $c_{\mathrm{r}}^* = 20$ we have $N_{\mathrm{min}} = 163$ and $N_{\mathrm{max}} = 15035$. The comparison also involves 3716 oblate spheroids, with parameters $a_x = a_y = 1000\,\mathrm{m}$ and $a_z \in [50, 950]\,\mathrm{m}$; all the other parameters are the same as those for the prolate sources. For oblate cavities, $c_{\mathrm{r}}^* = 10$ leads to $N_{\mathrm{min}} = 20$ and $N_{\mathrm{max}} = 1413$, and $c_{\mathrm{r}}^* = 20$ results in $N_{\mathrm{min}} = 163$ and $N_{\mathrm{max}} = 11410$. The convergence test involves 5868 triaxial ellipsoids, with parameters $x_0 = y_0 = 0\,\mathrm{m}$, $d_{\mathrm{C}} \in [1000, 2000]\,\mathrm{m}$, $a_x = 1000\,\mathrm{m}$, $a_y \in [50, 950]\,\mathrm{m}$, $a_z \in [50, 950]\,\mathrm{m}$ and $\omega_y \in [0°, 90°]$. For these ellipsoids the finite ECM solution with $c_{\mathrm{r}}^* = 12$ is compared to the solution with $c_{\mathrm{r}}^* = 20$. In all cases, the surface observation grid consists of 496 points with a spacing of 200 m within $x \in [-3000, 3000]\,\mathrm{m}$ and $y \in [0, 3000]\,\mathrm{m}$. For all sources $d_{\mathrm{T}} \geq 200\,\mathrm{m}$.

c_{r}^*	$\overline{t_C}$ [s]	$\max \epsilon_x$ [%]	$\max \epsilon_z$ [%]	$\alpha(\epsilon_x < 0.01)$ [%]	$\alpha(\epsilon_z < 0.01)$ [%]
			Prolate spheroids		
10	0.097	1.2	2.1	98.9	90.0
12	0.17	0.88	1.4	100	98.5
14	0.27	0.76	1.3	100	99.4
20	0.79	0.45	0.73	100	100
			Oblate spheroids		
10	0.10	3.4	4.9	85.0	53.0
12	0.17	2.7	3.5	87.7	80.0
14	0.27	2.1	2.8	99.5	91.3
20	0.80	0.9	1.3	100	99.8
			Ellipsoids		
12	0.40	1.5	2.8	99.7	95.7

half-space source models cannot be calculated analytically. One caveat is that the volume change for shallow sources in a half-space may be substantially different from the full-space volume change—accurate half-space volume change calculations require numerical methods (see Amoruso & Crescentini 2009; Anderson & Segall 2011). Since volume change and chamber compressibility may be important magma chamber properties both for inversions and for forward modeling of eruptive vol-

umes (Mastin et al. 2008; Anderson & Segall 2011; Wasser et al. 2021), we include codes based on the Eshelby (1957) approach for the accurate calculation of the full-space volume change and chamber compressibility (see Segall et al. 2001; Rivalta & Segall 2008; Segall 2010).

3 COMPARISON TO PUBLISHED ANALYTICAL AND NUMERICAL SOLUTIONS

We compare the finite ECM with published analytical and numerical solutions. Unless otherwise stated, we use $c_{\mathrm{r}}^{*} = 10$ and $N_{\max} = 4000$. Note that when comparing two solutions, displacements are commonly normalized in two different ways: I) Both solutions normalized by the maximum vertical displacement of one of the solutions; II) Each solution normalized by its own maximum vertical displacement. First, we compare the finite ECM with analytical solutions and next with numerical solutions for triaxial ellipsoids. We use normalization method I in our analytical comparisons (Fig. 2) and both normalization methods I and II in the numerical comparisons (Fig. 3). We later expand on the implications of the normalization methods.

As the first analytical source for the comparison we consider the Yang et al. (1988) spheroid depicted in Fig. 1a. Despite the rather high semi-major-axis to depth ratio of 0.95 for this case, the finite ECM agrees very well with the Yang et al. (1988) solution (Fig. 2a).

The second comparison (Fig. 2b) involves both the quadrupole solution for a finite ellipsoid by Amoruso & Crescentini (2011) and a prolate spheroid after Yang et al. (1988). All the solutions are identical in the far field, but in the near field the Amoruso & Crescentini (2011) solution substantially underestimates the surface displacements.

The next comparison involves the McTigue (1987) and Yang et al. (1988) solutions in the case of a sphere (Fig. 2c). The mismatch between the McTigue (1987) and the Yang et al. (1988) and finite ECM solutions is because the formulation of the latter solutions involves the same approximations as in the Davis et al. (1974) solution, while the McTigue (1987) solution contains higher-order terms correcting for the resulting misrepresentation of the boundary conditions on the cavity walls.

As the last analytical comparison, we consider a uniformly pressurized penny-shaped crack (Fialko et al. 2001), the Yang et al. (1988) solution and a horizontal tensile square dislocation (Davis 1983; Okada 1985). For this special case, the finite ECM has only one layer of point sources with different potencies. Again, there is an excellent agreement between the finite ECM and the Yang et al. (1988) solution. The difference with the Fialko et al. (2001) solution is due to the fact that the boundary conditions on the source walls are more accurately implemented in the Fialko et al. (2001) solution. However, compared to the square dislocation, the finite ECM and the Yang et al. (1988) solutions provide a better approximation to the Fialko et al. (2001) solution. This is because the opening of the square dislocation is uniform but the opening of the cracks represented by the Yang et al. (1988)

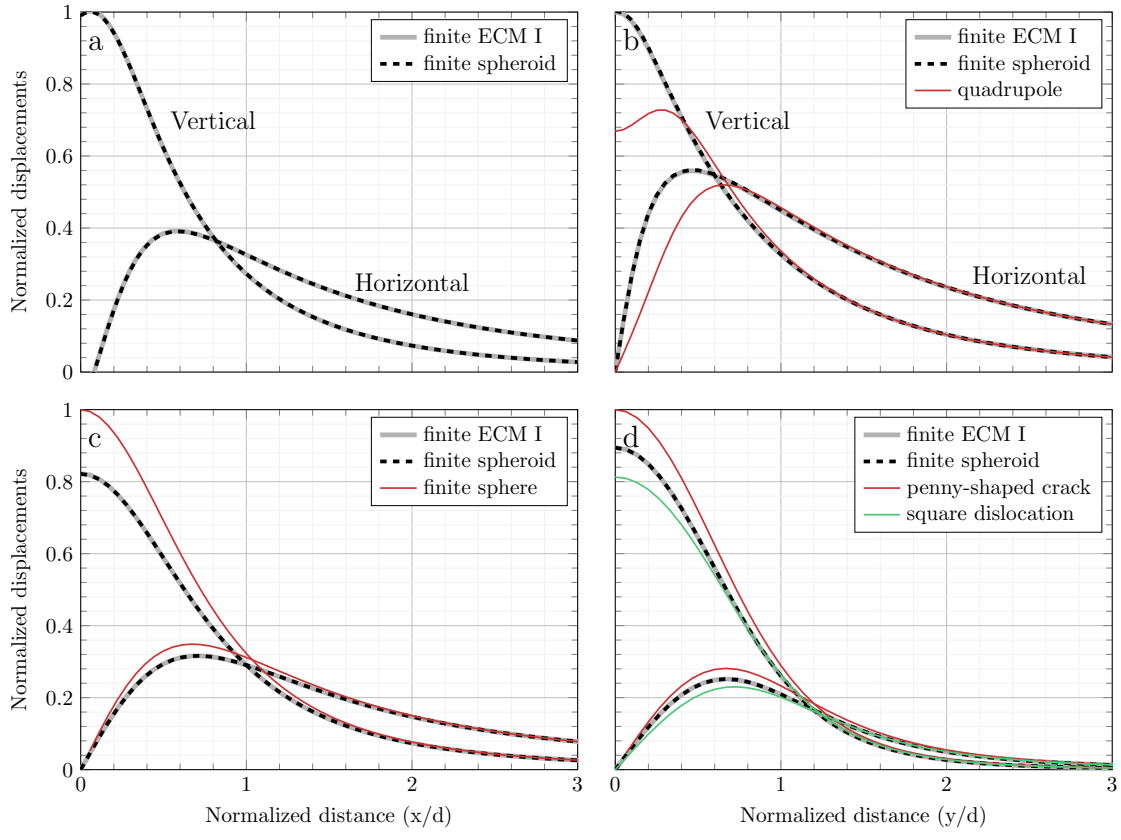

Figure 2. Comparison of the finite ECM with selected analytical solutions. In all panels the gray solid lines are the finite ECM displacements. For all displacements normalization method I has been used. a) Comparison with a spheroid (Yang et al. 1988). Source parameters are $a_x/a_z = 0.737$, $a_x = a_y$, $a_z/d_C = 0.950$ and $\omega_x = 0°$, $\omega_y = 15°$, $\omega_z = 150°$. The finite ECM is shown for $c_\mathrm{r}^* = 10$ which leads to $N = 4734$. The maximum relative error is well below 1 per cent. b) Comparison with the quadrupole solution (Amoruso & Crescentini 2011, red solid line) and a spheroid (Yang et al. 1988, black dashed line). Source parameters are $a_x/a_z = 0.333$, $a_x = a_y$, $a_z/d_C = 0.900$ and $\omega_x = \omega_y = \omega_z = 0°$. The finite ECM is shown for $c_\mathrm{r}^* = 10$ which leads to $N = 2571$. The maximum relative error is well below 1 per cent. c) Comparison with the finite spherical source by McTigue (1987, red solid line) and a spheroid (Yang et al. 1988, black dashed line). Source parameters are $a_x = a_y = a_z = R$ and $R/d_C = 0.556$. The finite ECM is shown for $c_\mathrm{r}^* = 14$ which leads to $N = 385$. The maximum relative error is well below 1 per cent. d) Comparison with the penny-shaped crack solution by Fialko et al. (2001, red solid line), a spheroid (Yang et al. 1988, black dashed line) and a square dislocation (Okada 1985, green dashed line). Source parameters are $a_z/a_x = 10^{-6}$, $a_x = a_y$, $a_x/d_C = 0.667$ and $\omega_x = \omega_y = \omega_z = 0°$. The finite ECM is shown for $c_\mathrm{r}^* = 10$ which leads to $N = 163$. The square dislocation has the same potency as the finite ECM and its edge length is $(\pi a_x^2)^{1/2}$.

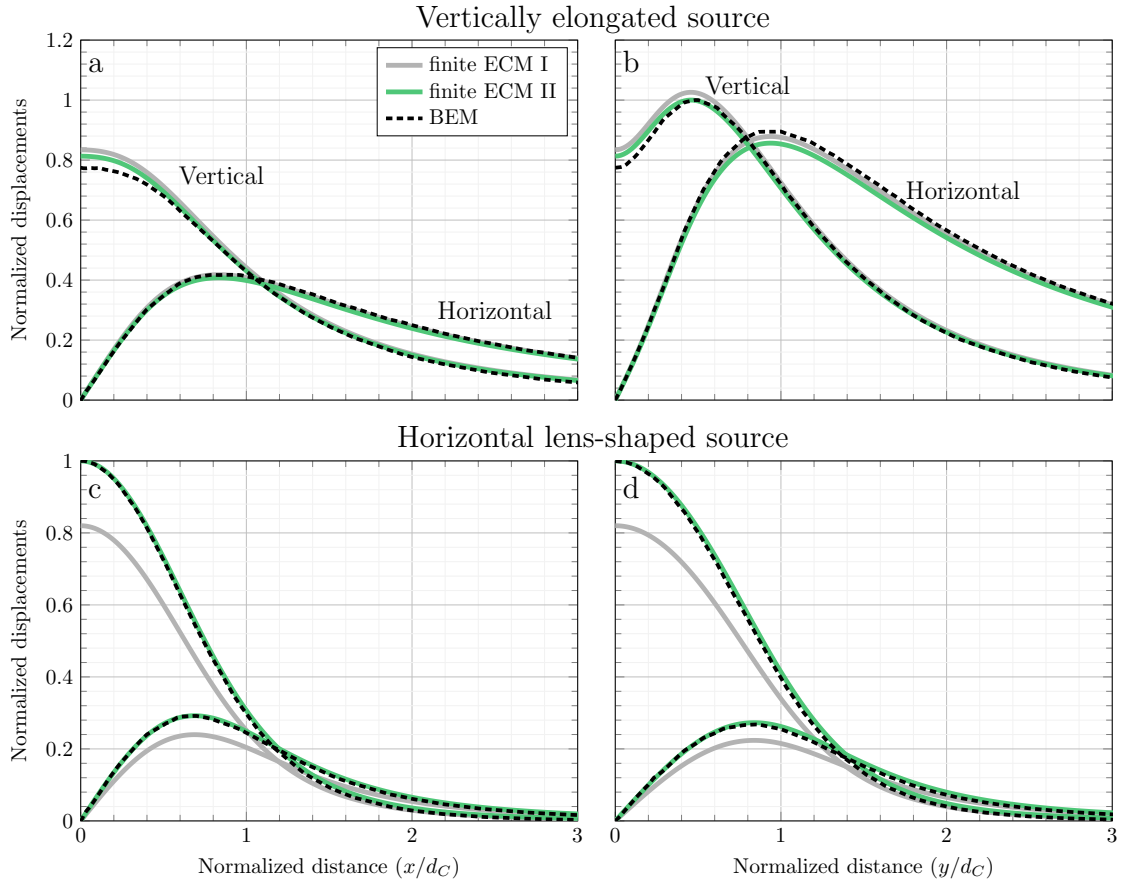

Figure 3. Comparison with selected numerical solutions for triaxial sources. The black dashed lines are BEM solutions from (Nikkhoo et al. 2017). The gray and green solid lines are the finite ECM displacements, normalized through methods I and II, respectively (see text). a) Vertically elongated source (Nikkhoo et al. 2017, Fig. 5) with $a_x = 0.75\,\text{km}$, $a_y = 0.5\,\text{km}$, $a_z = 1.5\,\text{km}$ and $d_C = 3\,\text{km}$. Displacements are shown for the xz plane. b) Same as a), but for the yz plane. c) Lens-shaped source (Nikkhoo et al. 2017, Fig. 7) with $a_x = 2\,\text{km}$, $a_y = 3\,\text{km}$, $a_z = 0.25\,\text{km}$ and $d_\text{C} = 3\,\text{km}$. Displacements are shown for the xz plane. d) Same as c), but for the yz plane. The finite ECM is shown for $c_\text{r}^* = 10$ which leads to $N = 90$ and $N = 527$ for the vertically elongated source (a and b) and the horizontal lens-shaped source (c and d), respectively.

solution and finite ECM have an elliptic form. This feature is implemented through step "7" of the adaptive algorithm.

Finally, we compare the surface displacements from the finite ECM and two triaxial ellipsoids calculated by Nikkhoo et al. (2017) using the Boundary Element Method (Fig. 3). For the vertically elongated cavity, we find that, except for the vertical displacements right above the ellipsoid, the solutions are nearly identical (Fig. 3a,b). The agreement is best along the y-axis, which is parallel to the semi-minor axis. For the second source, which is horizontal and lens-shaped, the agreement is not as good (Fig. 3c,d). However, the functional shape of the solutions is very similar: indeed, a substantially

better agreement is achieved if the displacements are normalized by method II (Fig. 3c,d). This implies that applying the finite ECM and Yang et al. (1988) solution to source inversions involving sill-like sources may lead to fairly good constraints on the source shape, but the volume change and depth of the source may be biased considerably.

4 DISCUSSION

We developed the finite ECM in the form of distributed point CDMs with the same aspect ratio determined through the Eshelby (1957) shape functions (eq. 1). Unless the cavity shape is spherical, spheroidal or crack-like, these functions involve elliptic integrals, which can be calculated only numerically. All other components of the finite ECM—all steps of the adaptive algorithm controlling the configuration of the solution—are analytical.

Yang et al. (1988) showed that due to using the Davis et al. (1974) half-space approximations in the derivation of their closed-form solution, it can accurately represent the surface displacements of a uniformly-pressurized cavity only if $d_{\mathrm{T}} \gtrsim \rho_{\mathrm{T}}$. The same empirical criterion applies to the finite ECM, because it also relies on the same Davis et al. (1974) half-space approximations. Note that the empirical criterion above was devised upon comparisons with finite element models for a few vertical spheroids only. A more general criterion for evaluating the accuracy of arbitrarily oriented ellipsoidal sources requires further comparisons with numerical solutions. We recommend including this criterion ($d_{\mathrm{T}} \gtrsim \rho_{\mathrm{T}}$) in inversions using the finite ECM in order to prevent calculations involving inaccurate solutions.

Among analytical volcano deformation sources, the McTigue (1987) and Fialko et al. (2001) solutions fulfill very accurately (although still not exactly) the uniform-pressure boundary conditions on the source walls. All the other available analytical source models, including Sun (1969); Yang et al. (1988); Amoruso & Crescentini (2011) and the finite ECM, make use of the Davis et al. (1974) half-space approximations. Therefore, inferring the parameters of uniformly pressurized magma bodies by using the latter group of source models may come with a substantial bias if the source is very shallow. An example of this can be seen in Fig. 3a-d, where a perfect fit is achieved for oblate sources, but with a biased volume change. As also shown by Amoruso & Crescentini (2011), such a bias is likely to emerge on depth and source aspect ratio, beside volume change. Similarly, biases on the spatial orientation of the source could be expected. The extent of these biases as a function of source depth and shape has not been thoroughly investigated yet and should be addressed by future studies.

The deformation signals measured at the Earth's surface can be used to infer some large-scale features of pressurized magma chambers. These large-scale features are in fact the deformation source parameters, which can be constrained through deformation modeling. For deep sources, these pa-

rameters are limited to the location, spatial orientation and strength; in this case point-source and finite-source models yield the same results. For shallow sources, in addition to the location, spatial orientation and strength, it is possible to constrain the source dimensions, provided that displacement data in the near-field are available. In this case, point-source solutions cannot be used because they cannot represent the displacements in the near field. Therefore, to infer the parameters of shallow magma chambers correctly, finite-source models need to be used. Among the available analytical finite-source solutions, the Yang et al. (1988) spheroid has the highest number of parameters, with full rotational degrees of freedom, but can only represent axi-symmetric deformation sources. The finite ECM is a triaxial source and therefore allows us to explore more general geometries in the plumbing systems of volcanoes.

5 CONCLUSIONS

1. We developed a computationally-efficient solution for the surface deformation field caused by a finite (triaxial) ellipsoidal source in the form of a non-uniform (depth-dependent) distribution of point CDMs. The finite ECM is especially suitable for inversions of surface deformation data.
2. The finite ECM includes an adaptive algorithm that determines the optimal spacing and location of the point CDMs as a function of the depth, shape, and spatial orientation of the cavity, and a grid-spacing parameter c_{r}^{*}.
3. We showed that the Yang et al. (1988) solution can be used to benchmark the finite ECM and calibrate c_{r}^{*}, or alternatively N_{max}, to achieve any desired accuracy while maintaining computation time minimal. We further validated the finite ECM through comparisons with other analytical and numerical solutions.
4. Deformation models such as the finite ECM and Yang et al. (1988) represent a uniformly-pressurized cavity only if the criterion $d_{\mathrm{T}} \gtrsim \rho_{\mathrm{T}}$ is fulfilled. Otherwise, biased parameters may be retrieved even if the model perfectly fits the surface displacements.
5. We provide MATLAB codes for the finite ECM and additional codes to calculate the volume change and chamber compressibility of ellipsoidal sources. The codes do not contain any MATLAB-specific function and it is straightforward to convert them to any other programming language.
6. In a separate work undertaken in parallel to the present paper, we show that the finite ECM can be used to simulate deformation-induced gravity changes associates with pressurized ellipsoidal cavities and also provide the respective MATLAB codes (Nikkhoo & Rivalta 2022).

APPENDIX A: ANALYTICAL SOLUTIONS FOR THE SHALLOWEST AND DEEPEST POINTS ON THE SURFACE OF A GENERIC ELLIPSOID

The standard ellipsoid $E_{\rm S}$ centered at the origin of a Cartesian xyz coordinate system has the form

$$\frac{x^2}{a_x^2}+\frac{y^2}{a_y^2}+\frac{z^2}{a_z^2}=1, \tag{A.1}$$

where the semi-axes a_x, a_y and a_z are aligned with the x, y and z coordinate axes, respectively. If (θ,λ) denote the spherical coordinates, of an arbitrary point P on the surface of $E_{\rm S}$, we have

$$\begin{aligned} x &= a_x \sin\theta\cos\lambda,\\ y &= a_y \sin\theta\sin\lambda,\\ z &= a_z \cos\theta, \end{aligned} \tag{A.2}$$

where $\theta\in[0,\pi]$ and $\lambda\in[0,2\pi)$. The matrices

$$R_x(\omega_x)=\begin{pmatrix} 1 & 0 & 0\\ 0 & \cos\omega_x & \sin\omega_x\\ 0 & -\sin\omega_x & \cos\omega_x \end{pmatrix}$$

$$R_y(\omega_y)=\begin{pmatrix} \cos\omega_y & 0 & -\sin\omega_y\\ 0 & 1 & 0\\ \sin\omega_y & 0 & \cos\omega_y \end{pmatrix},$$

$$R_z(\omega_z)=\begin{pmatrix} \cos\omega_z & \sin\omega_z & 0\\ -\sin\omega_z & \cos\omega_z & 0\\ 0 & 0 & 1 \end{pmatrix}, \tag{A.3}$$

represent general rotations about the x, y and z axes, respectively. Any arbitrary rotation in xyz can be represented in the form of

$$R=R_x(\omega_x)\,R_y(\omega_y)\,R_z(\omega_z)=\begin{pmatrix} r_{11} & r_{12} & r_{13}\\ r_{21} & r_{22} & r_{23}\\ r_{31} & r_{32} & r_{33} \end{pmatrix}, \tag{A.4}$$

with a unique set of angles $(\omega_x,\omega_y,\omega_z)$. After applying such a rotation, the new coordinates of P are

$$\begin{pmatrix} x'\\ y'\\ z' \end{pmatrix}=\begin{pmatrix} r_{11} & r_{12} & r_{13}\\ r_{21} & r_{22} & r_{23}\\ r_{31} & r_{32} & r_{33} \end{pmatrix}\begin{pmatrix} x\\ y\\ z \end{pmatrix}. \tag{A.5}$$

Combining equations A.5 and A.2 yields

$$z' = r_{31}a_x \sin\theta\cos\lambda + r_{32}a_y \sin\theta\sin\lambda + r_{33}a_z\cos\theta. \tag{A.6}$$

The spherical coordinates of the two points with the minimum and maximum z values on the ellipsoid are the solutions of the equation

$$\frac{\partial z'}{\partial\lambda} = 0, \quad \frac{\partial z'}{\partial\theta} = 0, \tag{A.7}$$

that can be written in explicit form as

$$\lambda = \operatorname{atan}\left(\frac{r_{32}a_y}{r_{31}a_x}\right), \quad \theta = \operatorname{atan}\left(\frac{r_{31}a_x + r_{32}a_y\tan\lambda}{r_{33}a_z\sqrt{1+\tan^2\lambda}}\right). \tag{A.8}$$

APPENDIX B: AN ANALYTICAL EXPRESSION FOR THE VOLUME OF A PARTITION OF AN ELLIPSOID BOUNDED BY TWO HORIZONTAL PLANES

Let C_P denote the ellipsoidal cap formed by the intersection of the standard ellipsoid, E_S (equation A.1) and an arbitrary plane, $S : Ax + By + Cz = D$, where the vector (A, B, C) is normal to the plane and points towards C_P. The volume of C_P is

$$V_\mathrm{P}(S) = \iiint_{C_\mathrm{P}} dxdydz. \tag{B.1}$$

In a new Cartesian XYZ coordinate system, where $x = a_xX$, $y = a_yY$ and $z = a_zZ$ the ellipsoid is mapped onto the unit sphere, $X^2 + Y^2 + Z^2 = 1$, and the plane is mapped onto the new plane $S' : Aa_xX + Ba_yY + Ca_zZ = D$. Also, equation B.1 can be rewritten as

$$V_\mathrm{P}(S) = V_\mathrm{P}(S') = a_xa_ya_z \iiint_{C'_\mathrm{P}} dXdYdZ, \tag{B.2}$$

where

$$\iiint_{C'_\mathrm{P}} dXdYdZ = \frac{1}{3}\pi(1-d_\mathrm{n})^2(2+d_\mathrm{n}), \tag{B.3}$$

is the volume of the spherical cap, C'_P, that is bounded by the unit sphere and the new plane (see Kern & Bland 1938, p. 37 and Harris & Stöcker 1998, p. 107) and $d_\mathrm{n} = D/(A^2a_x^2 + B^2a_y^2 + C^2a_z^2)^{1/2}$ is the shortest distance from the origin of XYZ to the new plane. Substituting equation B.3 in equation B.2 yields:

$$V_\mathrm{P}(S) = \frac{1}{3}\pi a_xa_ya_z(1-d_\mathrm{n})^2(2+d_\mathrm{n}). \tag{B.4}$$

Thus, the volume of the region inside E_S and bounded by two parallel planes $S_1 : Ax + By + Cz = D_1$ and $S_2 : Ax + By + Cz = D_2$ can be calculated as

$$V_{D_1D_2} = |V_\mathrm{P}(S_2) - V_\mathrm{P}(S_1)|. \tag{B.5}$$

For an arbitrary ellipsoid subjected to the rotations $R_x(\omega_x)R_y(\omega_y)R_z(\omega_z)$ and centered at $(x_0, y_0, -d)$, the volume of the region inside the ellipsoid and bounded by two horizontal planes $z = z_1$ and $z = z_2$ can be calculated from equation B.5 after applying the translation $(-x_0, -y_0, d)$ and rotations $R_z(-\omega_z)R_y(-\omega_y)R_x(-\omega_x)$ to the ellipsoid and both planes.

APPENDIX C: INTERSECTION OF A PLANE AND AN ARBITRARY ELLIPSOID

In order to determine the intersection ellipse associated with a horizontal plane, $S_{\rm H} : z = z_j$, and an arbitrary ellipsoid $E_{\rm R}$ subjected to the rotations $R_x(\omega_x)R_y(\omega_y)R_z(\omega_z)$ and centered at $(x_0, y_0, -d)$, we first apply the translation $(-x_0, -y_0, d)$ and rotations $R_z(-\omega_z)R_y(-\omega_y)R_x(-\omega_x)$ to both $E_{\rm R}$ and $S_{\rm H}$. These transformations lead to a standard ellipsoid $E_{\rm S}$ (equation A.1, and a plane of the form $S : Ax + By + Cz = D$. The intersection ellipse formed by $E_{\rm S}$ and S can be determined through the Klein (2012) formulas. Applying the rotations $R_x(\omega_x)R_y(\omega_y)R_z(\omega_z)$ and the translation $(x_0, y_0, -d)$ to the ellipse from the previous step yields the solution.

APPENDIX D: PRINCIPAL CURVATURES AT ANY POINT ON THE SURFACE OF AN ELLIPSOID

The principal curvatures, $\kappa_{\rm max}$ and $\kappa_{\rm min}$, at any point $P(\theta, \lambda)$ on the surface of the standard ellipsoid (equation A.1) are the solutions of the following equation:

$$(EG - F^2)\kappa^2 - (EN + GL - 2FM)\kappa + (LN - M^2) = 0, \tag{D.1}$$

where E, F and G are the first fundamental coefficients and L, M and N are the second fundamental coefficients of the ellipsoid (see Lipschutz 1969, p. 183). A simplified form of equation D.1 can be written as

$$A\kappa^2 + B\kappa + C = 0, \tag{D.2}$$

where

$$A = (a_x^2 \cos^2\theta \cos^2\lambda + a_y^2 \cos^2\theta \sin^2\lambda + a_z^2 \sin^2\theta)(a_x^2 \sin^2\lambda + a_y^2 \cos^2\lambda) - (a_y^2 - a_x^2)^2 \cos^2\theta \sin^2\lambda \cos^2\lambda,$$

$$B = \frac{-a_x a_y a_z}{q_n}(a_x^2 \cos^2\theta \cos^2\lambda + a_y^2 \cos^2\theta \sin^2\lambda + a_z^2 \sin^2\theta + a_x^2 \sin^2\lambda + a_y^2 \cos^2\lambda),$$

$$C = (a_x a_y a_z / q_n)^2, \tag{D.3}$$

in which

$$q_n = (a_y^2 a_z^2 \sin^2\theta \cos^2\lambda + a_x^2 a_z^2 \sin^2\theta \sin^2\lambda + a_x^2 a_y^2 \cos^2\theta)^{1/2}.$$

A singularity in equation D.1 at $\theta = 0$ has been addressed analytically in equation D.2. The maximum and minimum radii of curvature at P are

$$\rho_{\max} = 1/\kappa_{\min}, \quad \rho_{\min} = 1/\kappa_{\max}. \tag{D.4}$$

ACKNOWLEDGMENTS

This research was funded by the EU Horizon 2020 programme NEWTON-g project, under the FET-OPEN-2016/2017 call (Grant Agreement No 801221) and by the German Research Foundation (DFG), Grant 634756, RI 2782/2. We appreciate the hospitality and financial support of the ICTP solid earth geophysics group.

DATA AVAILABILITY

The MATLAB codes will be provided at http://www.volcanodeformation.com/ upon acceptance.

This paper has been produced using the Blackwell Scientific Publications GJI LaTeX2e class file.

REFERENCES

Amoruso, A. & Crescentini, L., 2009. Shape and volume change of pressurized ellipsoidal cavities from deformation and seismic data, *Journal of Geophysical Research: Solid Earth*, **114**(B2).

Amoruso, A. & Crescentini, L., 2011. Modelling deformation due to a pressurized ellipsoidal cavity, with reference to the campi flegrei caldera, italy, *Geophysical Research Letters*, **38**(1).

Amoruso, A. & Crescentini, L., 2013. Analytical models of volcanic ellipsoidal expansion sources, *Annals of Geophysics*, **56**(4), 0435.

Anderson, K. & Segall, P., 2011. Physics-based models of ground deformation and extrusion rate at effusively erupting volcanoes, *Journal of Geophysical Research: Solid Earth*, **116**(B7).

Battaglia, M., Cervelli, P. F., & Murray, J. R., 2013. dMODELS: A MATLAB software package for modeling crustal deformation near active faults and volcanic centers, *Journal of Volcanology and Geothermal Research*, **254**, 1–4.

Beauducel, F., Peltier, A., Villié, A., & Suryanto, W., 2020. Mechanical imaging of a volcano plumbing system from GNSS unsupervised modeling, *Geophysical Research Letters*, **47**(17), e2020GL089419.

Bonafede, M. & Ferrari, C., 2009. Analytical models of deformation and residual gravity changes due to a Mogi source in a viscoelastic medium, *Tectonophysics*, **471**(1-2), 4–13.

Cervelli, P. F., 2013. Analytical expressions for deformation from an arbitrarily oriented spheroid in a half-space, in *AGU Fall Meeting Abstracts*, vol. 2013, pp. V44C–06.

Davis, P., Hastie, L., & Stacey, F., 1974. Stresses within an active volcano—with particular reference to Kilauea, *Tectonophysics*, **22**(3-4), 355–362.

Davis, P. M., 1983. Surface deformation associated with a dipping hydrofracture, *Journal of Geophysical Research: Solid Earth*, **88**(B7), 5826–5834.

Davis, P. M., 1986. Surface deformation due to inflation of an arbitrarily oriented triaxial ellipsoidal cavity in an elastic half-space, with reference to Kilauea volcano, Hawaii, *Journal of Geophysical Research: Solid Earth*, **91**(B7), 7429–7438.

Dvorak, J. J. & Dzurisin, D., 1997. Volcano geodesy: The search for magma reservoirs and the formation of eruptive vents, *Reviews of Geophysics*, **35**(3), 343–384.

Dzurisin, D., 2003. A comprehensive approach to monitoring volcano deformation as a window on the eruption cycle, *Reviews of Geophysics*, **41**(1).

Eshelby, J. D., 1957. The determination of the elastic field of an ellipsoidal inclusion, and related problems, *Proceedings of the royal society of London. Series A. Mathematical and physical sciences*, **241**(1226), 376–396.

Fialko, Y., Khazan, Y., & Simons, M., 2001. Deformation due to a pressurized horizontal circular crack in an elastic half-space, with applications to volcano geodesy, *Geophysical Journal International*, **146**(1), 181–190.

Harris, J. W. & Stöcker, H., 1998. *Handbook of mathematics and computational science*, Springer Science & Business Media.

Kern, W. F. & Bland, J. R., 1938. *Solid mensuration: with proofs*, J. Wiley & Sons, Incorporated.

Klein, P. P., 2012. On the ellipsoid and plane intersection equation, *Applied Mathematics*, **3**(11), 1634–1640.

Lipschutz, M. M., 1969. *Schaum's outline of theory and problems of differential geometry*, McGraw-Hill, New York.

Lisowski, M., 2007. *Analytical volcano deformation source models*, pp. 279–304, Springer Berlin Heidelberg,

425 Berlin, Heidelberg.

426 Lisowski, M., Dzurisin, D., Denlinger, R. P., & Iwatsubo, E. Y., 2008. Analysis of GPS-measured deforma-
427 tion associated with the 2004–2006 dome-building eruption of Mount St. Helens, Washington, in *A Volcano*
428 *Rekindled: The Renewed Eruption of Mount St. Helens, 2004–2006*, vol. 1750, pp. 301–333, US Geological
429 Survey Reston, Virginia.

430 Mastin, L. G., Roeloffs, E., Beeler, N. M., & Quick, J. E., 2008. Constraints on the size, overpressure, and
431 volatile content of the Mount St. Helens magma system from geodetic and dome-growth measurements
432 during the 2004-2006+ eruption, Tech. rep., US Geological Survey.

433 McTigue, D., 1987. Elastic stress and deformation near a finite spherical magma body: resolution of the point
434 source paradox, *Journal of Geophysical Research: Solid Earth*, **92**(B12), 12931–12940.

435 Mindlin, R. D., 1936. Force at a point in the interior of a semi-infinite solid, *physics*, **7**(5), 195–202.

436 Mogi, K., 1958. Relations between the eruptions of various volcanoes and the deformations of the ground
437 surfaces around them, *Earthq Res Inst*, **36**, 99–134.

438 Nikkhoo, M. & Rivalta, E., 2022. Analytical solutions for gravity changes caused by triaxial volumetric
439 sources, *Accepted in Geophysical Research Letters*.

440 Nikkhoo, M., Walter, T. R., Lundgren, P. R., & Prats-Iraola, P., 2017. Compound dislocation models (CDMs)
441 for volcano deformation analyses, *Geophysical Journal International*, **208**(2), 877–894.

442 Okada, Y., 1985. Surface deformation due to shear and tensile faults in a half-space, *Bulletin of the seismolog-*
443 *ical society of America*, **75**(4), 1135–1154.

444 Rivalta, E. & Segall, P., 2008. Magma compressibility and the missing source for some dike intrusions,
445 *Geophysical Research Letters*, **35**(4).

446 Segall, P., 2010. *Earthquake and volcano deformation*, Princeton University Press.

447 Segall, P., Cervelli, P., Owen, S., Lisowski, M., & Miklius, A., 2001. Constraints on dike propagation from
448 continuous GPS measurements, *Journal of Geophysical Research: Solid Earth*, **106**(B9), 19301–19317.

449 Sun, R. J., 1969. Theoretical size of hydraulically induced horizontal fractures and corresponding surface
450 uplift in an idealized medium, *Journal of Geophysical Research (1896-1977)*, **74**(25), 5995–6011.

451 Wasser, V. K., Lopez, T. M., Anderson, K. R., Izbekov, P. E., & Freymueller, J. T., 2021. Multidisciplinary
452 Constraints on Magma Compressibility, the Pre-Eruptive Exsolved Volatile Fraction, and the H2O/CO2
453 Molar Ratio for the 2006 Augustine Eruption, Alaska, *Geochemistry, Geophysics, Geosystems*, **22**(9),
454 e2021GC009911.

455 Yang, X.-M., Davis, P. M., & Dieterich, J. H., 1988. Deformation from inflation of a dipping finite prolate
456 spheroid in an elastic half-space as a model for volcanic stressing, *Journal of Geophysical Research: Solid*
457 *Earth*, **93**(B5), 4249–4257.